ISSN 1749-3889 (print), 1749-3897 (online)
International Journal of Nonlinear Science
Vol.21(2016) No.3, pp.131-144

Estimation of Viscosity and Controller Strengthening in Boundary Stabilization of Korteweg-de Vries-Burgers' Equation

D. A. Garzon-Alvarado *, C.H. Galeano, J.M. Mantilla
Department of Mechanical and Mechatronic Engineering
National University of Colombia
(Received 16 May 2010, accepted 28 February 2015)

Abstract: This paper presents several numerical tests on reaction-diffusion equations in the Turing space, affected by convective fields present in incompressible flows under the Schnakenberg reaction mechanism. The tests are performed in 2D on square unit, to which we impose an advective field from the solution of the problem of the flow in a cavity. The model developed consists of a decoupled system of equations of reaction-advection-diffusion, along with the Navier-Stokes equations of incompressible flow, which is solved simultaneously using the finite element method. The results show that the pattern generated by the concentrations of the reacting system varies both in time and space due to the effect exerted by the advective field.

Keywords: reaction-convection-diffusion; turing instabilities; navier-Stokes; problem of the cavity

1 Introduction

Several physical problems can be modeled by balancing three factors: *diffusion*, *convection* and *reaction*[1]. The first is defined as the dispersion given in the species involved in the process throughout the physical domain of the problem. *Convection* is defined as the movement of species due to the fluid transport medium. And, for its part, the *reaction* is the process of interaction through which the species involved in the phenomenon are generated or consumed. Mathematically, the problem of reaction-advection-diffusion (RAD) can be expressed from the differential equation (1) together with the boundary conditions (2).

$$\frac{\partial u}{\partial t} + \mathbf{V} \cdot \nabla u = \nabla \cdot k \nabla u + Q(u) \tag{1}$$

$$\begin{array}{l} u = h(\mathbf{x}, t), \text{over } \Gamma_u \\ \nabla u = g(\mathbf{x}, t) \text{over } \Gamma_\nabla v \end{array} \tag{2}$$

where u is the concentration of the species studied, $\mathbf{V}$is the speed of the medium, $k$is the diffusion constant, $Q(u)$ the function that defines the reaction process, $h(\mathbf{x}, t)$ is the function that defines the values of $u$in a normal direction to the border Γ_u, and $g(\mathbf{x}, t)$ is the function that defines the gradient value of $u$along the border. The velocity $\mathbf{V}$can be impose "a priori" as in [2, 3] , or can be found, for example, by solving the Navier-Stokes system equations [4, 5] for incompressible flow proposed in (3):

$$\begin{array}{l} \rho \left(\frac{\partial \mathbf{V}}{\partial t} + \mathbf{V} \cdot \nabla \mathbf{V} \right) = -\nabla p + \mu \nabla^2 \mathbf{V} + \mathbf{f}, \\ \nabla \cdot \mathbf{V} = 0 \end{array} \tag{3}$$

where ρ is the fluid density, $p$is the pressure, μ is the viscosity and $\mathbf{f}$is the vector of body forces. These equations of reaction-advection-diffusion (RAD) (1) and other more complex models,where more species or reactants are involved, have the ability to create certain spatial-temporal patterns. A particular case of these patterns are*Turing instabilities* [1, 2], which are characterized by the appearance of species distributions (patterns), stable in time and unstable in space. Given their particular response, such models have inspired mathematical models for studying problems in many fields such as

*Corresponding author. *E-mail address*: dagarzona@bt.unal.edu.co

IJNS.2016.06.15/909

Table 1: Modes of vibration (m, n) for different values of d and γ of the Schnakenberg model with constant values $a = 0.1$ and $b = 0.9$[3]

Mode (m,n)	d	γ
(1,0)	10.0000	29.0000
(1,1)	11.5776	70.6000
(2,0)	10.0000	114.0000
(2,1)	9.1676	176.7200
(2,2)	8.6676	230.8200
(3,0)	8.6176	265.2200
(3,1)	8.6676	329.2000
(3,2)	8.8676	379.2100
(3,3)	8.6076	535.0900
(4,0)	8.6676	435.9900
(4,1)	8.5876	492.2800
(4,2)	8.7176	625.3500
(4,3)	8.6676	666.8200
(4,4)	8.6076	909.6600

fluid dynamics [6], heat transfer [7–9], physics of semiconductors[10], material engineering [11], chemistry[12], biology [13–15],population dynamics[16–18], astrophysics[19], biomedical engineering [20–22] and financial mathematics, among others [23–29].

Following the study of variation pattern by the action of convective fields from the numerical perspective, the objective of this paper is to solve computationally, and simultaneously, the equations of RAD and Navier-Stokes equations in 2D, for the Schnakenberg reaction system, with kinetic and diffusive parameters in Turing space.
To do this, we solve the RAD equation system through a conjunction approach of the finite element method and Newton-Raphson method [30]. As for the solution of the Navier-Stokes equations, we use a Petrov-Galerkin approach as shown in [31].

2 The model of reaction-advection-diffusion

2.1 Turing instability conditions

Following the Schnakenberg reagent model ([1],[3],[29]), the system of differential equations of RD in (1), can be written as (4):

$$\begin{array}{l} \frac{\partial u}{\partial t} + \mathbf{V} \cdot \nabla u - \nabla^2 u = \gamma(a - u + u^2 v) \ \ in \ \Omega \\ \frac{\partial v}{\partial t} + \mathbf{V} \cdot \nabla v - d\nabla^2 v = \gamma(b - u^2 v) \ \ in \ \Omega \end{array} \tag{4}$$

where u, v are the chemical species, $\nabla^2 u$ and $d\nabla^2 v$ are the diffusive terms, $d$is the relationship between the diffusive coefficients for each species, γ is a dimensionless constant, a and b are constant parameters of the model, $\mathbf{V}$is the velocity of the medium, while $f(u, v) = (a - u + u^2 v)$ and $g(u, v) = (b - u^2 v)$ are the Schnakenberg reaction functions.

The solution of this system of equations will lead to an unstable spatial distribution of concentrations or Turing patterns, if certain conditions are met, which for the case of a reaction-diffusion model, without convection, are given by the inequalities described in (5).

$$\begin{array}{l} f_u g_v - f_v g_u > 0 \\ f_u + g_v < 0 \\ d f_u + g_v > 0 \\ (d f_u + g_v)^2 > 4d\,(f_u g_v - f_v g_u) \end{array} \tag{5}$$

where $f_u = \frac{\partial f}{\partial u}$, $g_u = \frac{\partial g}{\partial u}$, $f_v = \frac{\partial f}{\partial v}$, $g_v = \frac{\partial g}{\partial v}$. Using the linear stability analysis [3], one can calculate the values of the dimensionless parameters d and γ, required for the formation of Turing patterns under the RD model. These patterns can be identified by the corresponding wave numbers as those listed in Table 1.

2.2 Solution by finite element of the RAD equations system

2.2.1 General considerations of the solution

To solve numerically the system of equations (4), we opted for an approach through the finite element method, using four-node bilinear elements[32]. Given the mathematical features of the problem, a solution was implemented with the following additional considerations:

Due to the nonlinearity of the reactive terms incorporated in the model, we used the Newton-Raphson method to solve the problem of temporal evolution of the species u and v.

The value of the velocity term $\mathbf{V}$ used in the iteration n in the approximation of the RAD equation, was the value calculated at time $n-1$in the solution of the Navier-Stokes equations. The time integration has been made using the trapezoidal rule and a fully implicit formulation.

2.2.2 Formulation of the equation of weighted residues and weak form

Initially raising the weighted residue equation for the system of differential equations (4), we obtain:

$$\begin{array}{l} \int\limits_{\Omega} w_1 \left(\frac{\partial u}{\partial t} + \mathbf{V}\cdot\nabla u - \nabla^2 u - \gamma(a-u+u^2v)\right)d\Omega = 0 \\ \int\limits_{\Omega} w_2 \left(\frac{\partial v}{\partial t} + \mathbf{V}\cdot\nabla v - d\nabla^2 v - \gamma(b-u^2v)\right)d\Omega = 0 \end{array} \tag{6}$$

where Ω refers to the problem domain, which is limited by the borderΓ,while w_1 and w_2 are weighting functions. Using Green's theorem to the weakening of the equations (6), gives:

$$\int\limits_{\Omega} w_1 \frac{\partial u}{\partial t} d\Omega + \int\limits_{\Omega} w_1 \mathbf{V}\cdot\nabla u d\Omega + \int\limits_{\Omega} \nabla w_1 \nabla u d\Omega - \int\limits_{\Omega} \gamma w_1 (a-u+u^2v) d\Omega - \int_{\Gamma} (\nabla u \cdot n)\, w_1 d\Gamma = 0 \tag{7}$$

$$\int\limits_{\Omega} w_2 \frac{\partial v}{\partial t} d\Omega + \int\limits_{\Omega} w_2 \mathbf{V}\cdot\nabla v d\Omega + \int\limits_{\Omega} \nabla w_2 . d\nabla v d\Omega - \int\limits_{\Omega} \gamma w_2 (b-u^2v) d\Omega - \int_{\Gamma} (\nabla v \cdot n)\, w_2 d\Gamma = 0 \tag{8}$$

From the equations of weighted residues in its weak form (7)(8), we can propose the residues of the problem, as follows:

$$\begin{array}{l} r_u = \int_\Omega w_1 \frac{\partial u}{\partial t} d\Omega + \int_\Omega w_1 \mathbf{V}\cdot\nabla u d\Omega + \int_\Omega \nabla w_1 \nabla u d\Omega - \int_\Omega \gamma w_1 a d\Omega + \int_\Omega \gamma w_1 u d\Omega \\ - \int_\Omega \gamma w_1 u^2 v d\Omega - \int_\Gamma w_1 (\nabla u \cdot n)\, d\Gamma = 0 \\ r_v = \int_\Omega w_2 \frac{\partial v}{\partial t} d\Omega + \int_\Omega w_2 \mathbf{V}\cdot\nabla v d\Omega + \int_\Omega \nabla w_2 \nabla v d\Omega - \int_\Omega \gamma b w_2 d\Omega \\ + \int_\Omega \gamma w_2 u^2 v d\Omega - \int_\Gamma w_2 (\nabla v \cdot n)\, d\Gamma = 0 \end{array} \tag{9}$$

Defining zero flow conditions or homogeneous Neumann conditions on the contours of the problem, the terms related to boundary integral equations (9) are canceled, and then the residues are now expressed as:

$$\begin{array}{l} r_u = \int_\Omega w_1 \frac{\partial u}{\partial t} d\Omega + \int_\Omega w_1 \mathbf{V}\cdot\nabla u d\Omega + \int_\Omega \nabla w_1 \nabla u d\Omega - \int_\Omega \gamma a w_1 d\Omega + \int_\Omega \gamma w_1 u d\Omega \\ - \int_\Omega \gamma w_1 u^2 v d\Omega = 0 \\ r_v = \int_\Omega w_2 \frac{\partial v}{\partial t} d\Omega + \int_\Omega w_2 \mathbf{V}\cdot\nabla v d\Omega + \int_\Omega \nabla w_2 \nabla v d\Omega - \int_\Omega \gamma b w_2 d\Omega + \int_\Omega \gamma w_2 u^2 v d\Omega = 0 \end{array} \tag{10}$$

To raise the discrete solution, we implemented written approximations as the linear combination of orthogonal functions, such as proposed in (11) [32, 34], where these approximation functions will have the same form of the weighting functions$w$. So then, variables u and $k$are written in terms of nodal values using the approximation functions $\mathbf{N}$, thus:

$$\begin{array}{l} u^h = \mathbf{N_u}(x,y)\mathbf{u} \\ v^h = \mathbf{N_v}(x,y)\mathbf{v} \\ V^h = \mathbf{N_V}(x,y)\mathbf{V} \end{array} \tag{11}$$

where $\mathbf{N_u}(x,y)$, $\mathbf{N}_v(x,y)$, $\mathbf{N}_V(x,y)$are the shape functions, which depend only on the space used for formulation, $\mathbf{u}$ and $\mathbf{v}$ are the values of $u$and$v$ at the nodal points, while the superscript h indicates that discretization of the variable in finite elements. Note that the use of weighting functions w with the same form as the functions of approximation $\mathbf{N}$, indicate the use of Bubnov-Galerkin formulation, instead of a SUPG formulation, capable of stabilizing the numerical problems arising from the inclusion of advective terms. This selection is based on the size of the mesh used in all simulated

problems, which ensures obtaining Peclet numbers less than unity, which guarantees that even with the Bubnov-Galerkin formulation, conventional solutions can be obtained numerically stable [35].

By substitution of (11) in (10) yields the residual vector in its discrete form (12), where $\underline{r_u^h}$ and $\underline{r_v^h}$ are vectors of residue for each equation and $\nabla \mathbf{N}$ is the vector gradient of the approximation functions.

$$\begin{array}{l} \underline{r_u^h} = \int_\Omega \mathbf{N}^T \frac{\partial u^h}{\partial t} d\Omega + \int_\Omega \mathbf{N}^T \left(\mathbf{V}^h \cdot \nabla u^h\right) d\Omega + \int_\Omega \nabla \mathbf{N}^T \nabla u^h d\Omega - \int_\Omega \gamma a \mathbf{N}^T d\Omega + \int_\Omega \gamma \mathbf{N}^T u^h d\Omega \\ \quad - \int_\Omega \gamma \mathbf{N}^T \left(u^h\right)^2 v^h d\Omega \\ \underline{r_v^h} = \int_\Omega \mathbf{N}^T \frac{\partial v^h}{\partial t} d\Omega + \int_\Omega \mathbf{N}^T \left(\mathbf{V}^h \cdot \nabla v^h\right) d\Omega + \int_\Omega \nabla \mathbf{N}^T d\nabla v^h d\Omega - \int_\Omega \gamma b \mathbf{N}^T d\Omega + \int_\Omega \gamma \mathbf{N}^T \left(u^h\right)^2 v^h d\Omega \end{array} \tag{12}$$

Using a temporal discretization base on the Crank-Nicolson equation [35], equation (12) becomes (13). In the latter expression $\tilde{u}^h$and $\tilde{v}^h$are the nodal values u^h and v^h evaluated over time $t + \Delta t$, while α is a characteristic parameter of the method of time integration ([32],[34],[35]).

$$\begin{array}{l} \underline{r_u^h} = \int_\Omega \mathbf{N}^T \frac{\left(\tilde{u}^h - u^h\right)}{\Delta t} d\Omega + \alpha \left(\begin{array}{l} \int_\Omega \mathbf{N}^T \left(\mathbf{V}^h \cdot \nabla \tilde{u}^h\right) d\Omega + \int_\Omega \nabla \mathbf{N}^T \nabla \tilde{u} d\Omega - \int_\Omega \gamma a \mathbf{N}^T d\Omega \\ + \int_\Omega \gamma \mathbf{N}^T \tilde{u}^h d\Omega - \int_\Omega \gamma \mathbf{N}^T \left(\tilde{u}^h\right)^2 \tilde{v}^h d\Omega \end{array} \right)^{t+\Delta t} \\ + (1-\alpha) \left(\begin{array}{l} \int_\Omega \mathbf{N}^T \left(\mathbf{V}^h \cdot \nabla u^h\right) d\Omega + \int_\Omega \nabla \mathbf{N}^T \nabla u^h d\Omega - \int_\Omega \gamma a \mathbf{N}^T d\Omega \\ + \int_\Omega \gamma \mathbf{N}^T u^h d\Omega - \int_\Omega \gamma \mathbf{N}^T \left(u^h\right)^2 v^h d\Omega \end{array} \right)^{t} \\ \underline{r_v^h} = \int_\Omega \mathbf{N}^T \frac{\left(V^h - v^h\right)}{\Delta t} d\Omega + \alpha \left(\begin{array}{l} \int_\Omega \mathbf{N}^T \left(\mathbf{V}^h \cdot \nabla \tilde{v}^h\right) d\Omega + \int_\Omega \nabla \mathbf{N}^T d\nabla \tilde{v}^h d\Omega - \int_\Omega \gamma b \mathbf{N}^T d\Omega \\ + \int_\Omega \gamma \mathbf{N}^T \left(\tilde{u}^h\right)^2 \tilde{v}^h d\Omega \end{array} \right)^{t+\Delta t} \\ + (1-\alpha) \left(\begin{array}{l} \int_\Omega \mathbf{N}^T \left(\mathbf{V}^h \cdot \nabla v^h\right) d\Omega + \int_\Omega \nabla \mathbf{N}^T d\nabla v^h d\Omega - \int_\Omega \gamma b \mathbf{N}^T d\Omega \\ + \int_\Omega \gamma \mathbf{N}^T \left(u^h\right)^2 v^h d\Omega \end{array} \right)^{t} \end{array} \tag{13}$$

Using expressions (13) we can calculate each of the terms of the tangent stiffness matrix, shown in (14).

$$\begin{array}{l} \frac{\partial r_u^h}{\partial \tilde{\mathbf{u}}} = \frac{1}{\Delta t} \int_\Omega \mathbf{N}^T \mathbf{N} d\Omega + \alpha \left(\begin{array}{l} \int_\Omega \mathbf{N}^T \left(\mathbf{V}^h \cdot \nabla \mathbf{N}\right) d\Omega + \int_\Omega \nabla \mathbf{N}^T \nabla \mathbf{N} d\Omega + \int_\Omega \gamma \mathbf{N}^T \mathbf{N} d\Omega \\ - \int_\Omega \gamma \mathbf{N}^T \left(2\tilde{u}^h\right) \tilde{v}^h \mathbf{N} d\Omega \end{array} \right) \\ \frac{\partial r_u^h}{\partial \tilde{\mathbf{v}}} = -\alpha \int_\Omega \mathbf{N}^T \gamma \left(\tilde{u}^h\right)^2 \mathbf{N} d\Omega \\ \frac{\partial r_v^h}{\partial \tilde{\mathbf{u}}} = \alpha\gamma \int_\Omega \mathbf{N}^T \left(2\tilde{u}^h\right) \tilde{v}^h \mathbf{N} d\Omega \\ \frac{\partial r_v^h}{\partial \tilde{\mathbf{v}}} = \frac{1}{\Delta t} \int_\Omega \mathbf{N}^T \mathbf{N} d\Omega + \alpha \left(\int_\Omega \mathbf{N}^T \left(\mathbf{V}^h \cdot \nabla \mathbf{N}\right) d\Omega + d \int_\Omega \nabla \mathbf{N}^T \nabla \mathbf{N} d\Omega + \int_\Omega \mathbf{N}^T \gamma \left(\tilde{u}^h\right)^2 \mathbf{N} d\Omega \right) \end{array} \tag{14}$$

It should be noted, that for purposes of simplicity in the simultaneous solution of the RAD and the Navier-Stokes equations, the nodal velocity terms V^hused in equation (14) correspond to the passage of time $t$and not to $t + \Delta t$. However this simplification does not imply any loss of accuracy because the two systems of equations, which are solved simultaneously and are found uncoupled. Thus, the nodal values u^h and v^hin time $t + \Delta t$can be approximated by a Newton-Raphson iterative algorithm, as described in equation (15), where Δu^h and Δv^hrepresent the difference of the nodal values in two consecutive iterations

$$\begin{bmatrix} \frac{\partial r_u^h}{\partial \tilde{\mathbf{u}}} & \frac{\partial r_u^h}{\partial \tilde{\mathbf{v}}} \\ \frac{\partial r_v^h}{\partial \tilde{\mathbf{u}}} & \frac{\partial r_v^h}{\partial \tilde{\mathbf{v}}} \end{bmatrix} \begin{bmatrix} \Delta u^h \\ \Delta v^h \end{bmatrix} = \begin{bmatrix} \underline{r_u^h} \\ \underline{r_v^h} \end{bmatrix} \tag{15}$$

2.3 Solution for the Navier-Stokes equations

2.3.1 General considerations of the solution

Following are presented the expressions used for the numerical solution of the Navier-Stokes equations (3), which will provide the required information on behavior of the advective field of velocities. A first step towards solving the problem, consists in the linearization of the equations (3), as suggested in (16):

$$\begin{cases} \rho \left(\frac{\partial \mathbf{V}^t}{\partial t} + \mathbf{V}^{t-\Delta t} \cdot \nabla \mathbf{V}^t \right) = -\nabla p + \mu \nabla^2 \mathbf{V}^t + \mathbf{f}, \\ \nabla \cdot \mathbf{V}^t = 0 \end{cases} \tag{16}$$

$$\begin{cases} \rho\left(\frac{\partial \mathbf{V}^t}{\partial t} + \mathbf{V}^{t-\Delta t}\cdot\nabla\mathbf{V}^t\right) = -\nabla p + \mu\nabla^2\mathbf{V}^t + \mathbf{f}, \\ \nabla\cdot\mathbf{V}^t = 0 \end{cases} \tag{16}$$

where the superscript refers to the passage of time in which each term is evaluated. As shown in (16), the original nonlinear term $\mathbf{V}^t\cdot\nabla\mathbf{V}^t$was linearized evaluating one of the factors in the previous time step. It should be noted that the effect of linearizing the convective term introduces restrictions of the temporary progress (size of the time step).

Additionally, it should be noted that, to meet the criteria of incompressibility, without coming up with formulations with terms of stabilization for this purpose, we used a mixed solution of quadrilateral elements, which involves nine nodes for calculating velocities and four for the calculation of the pressures ([16],[31]).

2.3.2 Formulation by finite elements

Following a similar approach used in [31] we carried out the system solution of Navier-Stokes equations. Thus, the numerical approach stabilized using SUPG, leads to the matrix system (17):

$$\begin{bmatrix} K+C+M_m & G \\ L-G^T & M \end{bmatrix}\begin{bmatrix} \mathbf{V} \\ \mathbf{p} \end{bmatrix} = \begin{bmatrix} F \\ H \end{bmatrix} \tag{17}$$

where $\mathbf{V}$is the vector of unknown nodal velocities at the new time step (we have omitted the superscript t), $\mathbf{p}$is the pressure vector calculated for the passage of time t, K, is the matrix of viscosity, $G$is the gradient matrix, $G^T$is the matrix of divergence, $M_m$is the mass matrix, C is the convective matrix, $M$the matrix of stabilization and $L$is the matrix of consistency [31]. The definition of each of the matrices included in the expression (17), are calculated as shown in (18) and (19) [31].

$$\begin{cases} \mathbf{K} = \underset{e=1}{\overset{n_{el}}{A}}(\mathbf{k}^e) & \mathbf{G} = \underset{e=1}{\overset{n_{el}}{A}}(\mathbf{g}^e) & \mathbf{L} = \underset{e=1}{\overset{n_{el}}{A}}(\mathbf{l}^e) & \mathbf{M_m} = \underset{e=1}{\overset{n_{el}}{A}}(\mathbf{m}_m^e) \\ \mathbf{M} = \underset{e=1}{\overset{n_{el}}{A}}(\mathbf{m}^e) & \mathbf{F} = \underset{e=1}{\overset{n_{el}}{A}}(\mathbf{f}^e) & \mathbf{H} = \underset{e=1}{\overset{n_{el}}{A}}(\mathbf{h}^e) & \mathbf{C} = \underset{e=1}{\overset{n_{el}}{A}}(\mathbf{c}^e) \end{cases} \tag{18}$$

where $\underset{e=1}{\overset{n_{el}}{A}}$ denotes the operator of assembly of global matrices from the elementary matrices, which are defined in (19). The vectors involved in the calculation of the elementary matrices (19), are defined by the terms described in (20).

$$\begin{cases} \mathbf{k}^e = \underset{\Omega^e}{\int}\left(\mathbf{B}^V\right)^T\mathbf{D}\mathbf{B}^V d\Omega; \\ \mathbf{m}^e = \frac{\alpha^e(h^e)^2}{2\mu}\underset{\Omega^e}{\int}\left(\mathbf{B}_2^P\right)^T\mathbf{B}_2^P d\Omega; \\ \mathbf{c}^e = \underset{\Omega^e}{\int}\left(\mathbf{N}^V\right)^T\mathbf{V}^{t-\Delta t}\mathbf{N}_\mathbf{d}^\mathbf{V} d\Omega; \\ \mathbf{f^e} = \frac{1}{\Delta t}\underset{\Omega^e}{\int}\left(\mathbf{N}^V\right)^T\mathbf{V}^{t-\Delta t}d\Omega + \underset{\Omega^e}{\int}\left(\mathbf{N}^V\right)^T\mathbf{f}d\Omega + \underset{\Gamma_N}{\int}\left(\mathbf{N}_d^V\right)^T\mathbf{h}d\Gamma_N \\ \mathbf{g}^e = -\underset{\Omega^e}{\int}\left(\mathbf{N}_\mathbf{d}^\mathbf{V}\right)^\mathbf{T}\mathbf{N}^P d\Omega \\ \mathbf{l}^e = -\frac{\alpha^e(h^e)^2}{2}\underset{\Omega^e}{\int}\left(\mathbf{B}_2^P\right)^T\left(\mathbf{B}_3^V + \mathbf{B}_4^V\right)d\Omega \\ \mathbf{m_m^e} = \frac{1}{\Delta t}\underset{\Omega^e}{\int}\left(\mathbf{N}^V\right)^T\mathbf{N}^V d\Omega \\ \mathbf{h^e} = \frac{\alpha^e(h^e)^2}{2\mu}\underset{\Omega^e}{\int}\left(\mathbf{B}_2^P\right)^T\mathbf{f}d\Omega \end{cases} \tag{19}$$

$$
\begin{cases}
\mathbf{B}^V = \left[\begin{array}{cccc} \mathbf{B}_1^V| & \mathbf{B}_2^V| & ...| & \mathbf{B}_{n_V}^V \end{array} \right] & \mathbf{B}_i^V = \left[\begin{array}{ccc} \frac{\partial N_i^V}{\partial x} & 0 & \frac{\partial N_i^V}{\partial y} \\ 0 & \frac{\partial N_i^V}{\partial y} & \frac{\partial N_i^V}{\partial x} \end{array} \right]^T \\
\mathbf{B_2^p} = \left[\begin{array}{cccc} \mathbf{B}_{\mathbf{2}_1}^{\mathbf{p}}| & \mathbf{B}_{\mathbf{2}_2}^{\mathbf{p}}| & ...| & \mathbf{B}_{\mathbf{2}_{n_p}}^{\mathbf{p}} \end{array} \right] & \mathbf{B}_{\mathbf{2_i}}^{\mathbf{p}} = \left[\begin{array}{cc} \frac{\partial N_i^P}{\partial x} & \frac{\partial N_i^P}{\partial y} \end{array} \right]^T \\
\mathbf{B}_3^{\mathbf{V}} = \left[\begin{array}{cccc} \mathbf{B}_{\mathbf{3}_1}^{\mathbf{V}}| & \mathbf{B}_{\mathbf{3}_2}^{\mathbf{V}}| & ...| & \mathbf{B}_{\mathbf{3}_{n_V}}^{\mathbf{V}} \end{array} \right] & \mathbf{B}_{\mathbf{3}_i}^{\mathbf{V}} = \left[\begin{array}{cc} \frac{\partial^2 N_i^V}{\partial x^2} + \frac{\partial^2 N_i^V}{\partial y^2} & 0 \\ 0 & \frac{\partial^2 N_i^V}{\partial x^2} + \frac{\partial^2 N_i^V}{\partial y^2} \end{array} \right] \\
\mathbf{B}_4^{\mathbf{V}} = \left[\begin{array}{cccc} \mathbf{B}_{4_1}^{\mathbf{V}}| & \mathbf{B}_{4_2}^{\mathbf{V}}| & ...| & \mathbf{B}_{4_{n_V}}^{\mathbf{V}} \end{array} \right] & \mathbf{B}_{4_i}^{\mathbf{V}} = \left[\begin{array}{cc} \frac{\partial^2 N_i^V}{\partial x^2} & \frac{\partial^2 N_i^V}{\partial x \partial y} \\ \frac{\partial^2 N_i^V}{\partial x \partial y} & \frac{\partial^2 N_i^V}{\partial y^2} \end{array} \right] \\
\mathbf{N^V} = \left[\begin{array}{cccc} \mathbf{N}_1^{\mathbf{V}}| & \mathbf{N}_2^{\mathbf{V}}| & ...| & \mathbf{N}_{n_V}^{\mathbf{V}} \end{array} \right] & \mathbf{N_i^V} = \left[\begin{array}{cc} N_i^V & N_i^V \end{array} \right]^T \\
\mathbf{N_d^V} = \left[\begin{array}{cccc} \mathbf{N}_{\mathbf{d}_1}^{\mathbf{V}}| & \mathbf{N}_{\mathbf{d}_2}^{\mathbf{V}}| & ...| & \mathbf{N}_{\mathbf{d}_{n_V}}^{\mathbf{V}} \end{array} \right] & \mathbf{N}_{\mathbf{d_i}}^{\mathbf{V}} = \left(\begin{array}{cc} \frac{\partial N_i^V}{\partial x} & \frac{\partial N_i^V}{\partial y} \end{array} \right)
\end{cases} \tag{20}
$$

In this last set of expressions, N_i^V are the shape functions that interpolate the velocity, while N_i^P are the shape functions that interpolated the pressure. Moreover, $n_V$is the number of nodes used for interpolation of the velocity function and $n_P$is the number of nodes used for interpolation of the pressure function.

2.4 Computational solution

We propose to analyze the formation of Turing patterns in a square domain of unit length, considering a reactive process characterized by the Schnakenberg equation and an advective field associated to the flow inside the cavity ([31],[36],[37]), this problem is defined by equations (1) and (3). To finish defining the problem, we considered as boundary conditions for RAD equations a null flow conditions (homogeneous Neumann conditions). Meanwhile, in the case of the Navier-Stokes equations were considered zero velocity conditions on all borders of the cavity, except the top, where it has been imposed a horizontal velocity $V_X = c(t)$. Figure 1 summarizes each of these conditions.

As for the initial conditions, we did tests with two different types of initial conditions. The first type of initial condition consisted of the steady state of reactive-diffusive problem, while the second type of initial condition was based on a disturbance of the homogeneous steady state of each of the reactive terms, as described in (21).

$$
\begin{cases}
u(x, y, t = 0) = u_s + \varepsilon u_s \\
v(x, y, t = 0) = v_s + \varepsilon v_s \\
(u_s, v_s) = \left(a + b, \frac{b}{(a+b)^2} \right)
\end{cases} \tag{21}
$$

where $f(u_s, v_s) = 0$and $g(u_s, v_s) = 0$,are the steady states of the reactive terms and ε is a random perturbation parameter.

As mentioned above, the discretization used consisted in bilinear quadrilateral elements of four nodes for the problem of RAD, and a mixed formulation for the Navier-Stokes problem, which consisted of elements of 9 nodes (quadratic quadrilateral element [32]) for the interpolation of the velocity and 4 nodes (bilinear quadrilateral [32]) for the interpolation of pressure (see Figure 2).

To perform the numerical implementation we programmed the set of equations in FORTRAN language and solved all the examples that are illustrated below in a Laptop of 4096 MB in RAM and 800 MHz processor speed.

The mesh used is the same for all examples (see Figure 3), which consists of 2500 quadrilateral 4-node elements for the interpolation of the pressure and the concentrations u and v (for a total of 2601 nodes); and the same number of elements but for 9 nodes, for the interpolation of velocity components (for a total of 10,201 nodes).

For the time integration we used a step $\Delta t = 0.01$ and as convergence criterion of nonlinear problem (Newton-Raphson), we used a relative error control of convergence $\|TOL\| \leqslant 10^{-14}$[30].

3 Results

Following below we present the results obtained through numerical formulation by finite element raised earlier. In first instance we will show the results related to the advective velocity field, and then present the results of the RAD system, considering a convective term imposed by the temporal evolution of the previously calculated velocity field. For brevity,

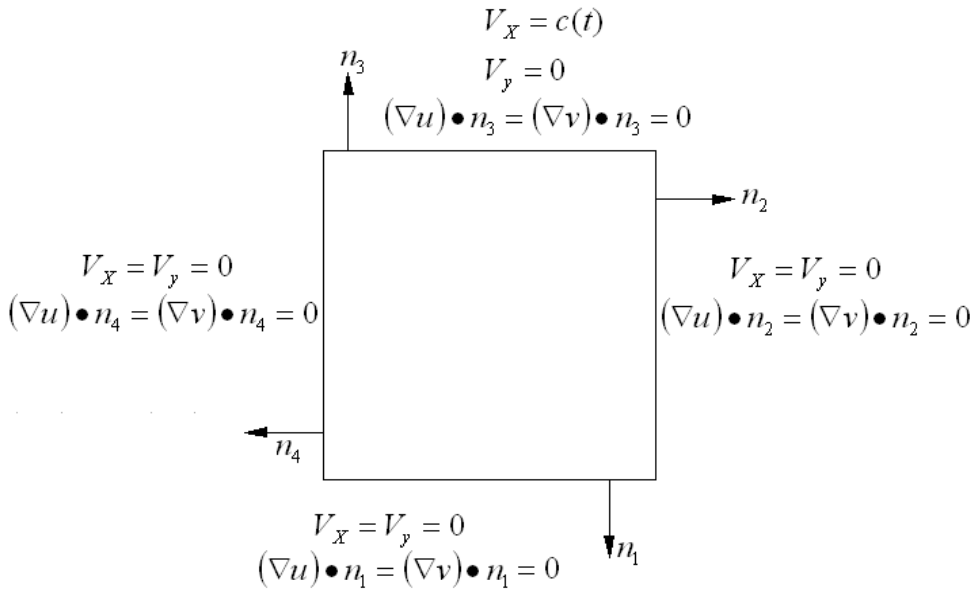

Figure 1: Boundary conditions for the problem of Navier-Stokes and advection-diffusion-reaction. n_i indicates the normal to each side of the unit square

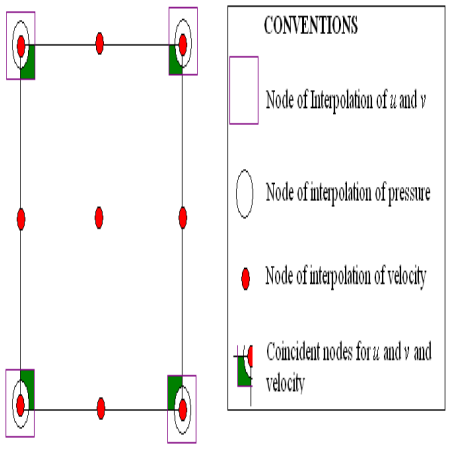

Figure 2: Interpolation points for each variable (conventions in the figure). This element is quadrilateral and reference (for details see [32]).

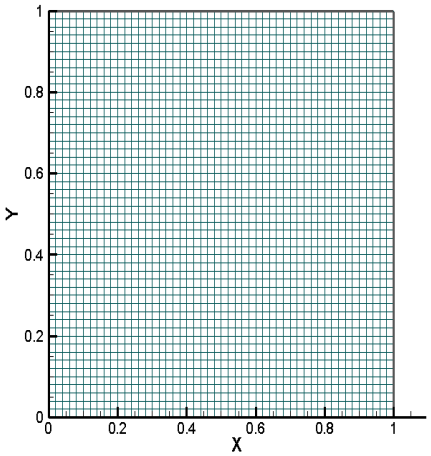

Figure 3: Mesh used in the numerical solution. The mesh has 2500 elements and 2601 nodes (bilinear case) to interpolate the pressure and concentrations of the reactive system, and 10201 nodes (quadratic case) to interpolate the velocity.

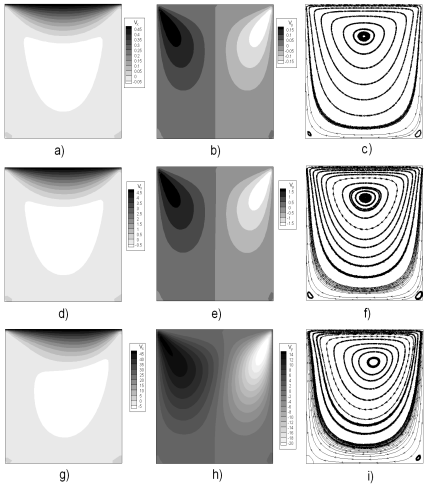

Figure 4: Results for the solution of the cavity problem for an incompressible flow with different velocity values. a), d) and g) show the results for the velocity in x with Reynolds numbers of 0.5, 5 and 50, respectively. b), e) and h) show the results for the velocity in y and, c), f) and i) show the results for the streamlines.

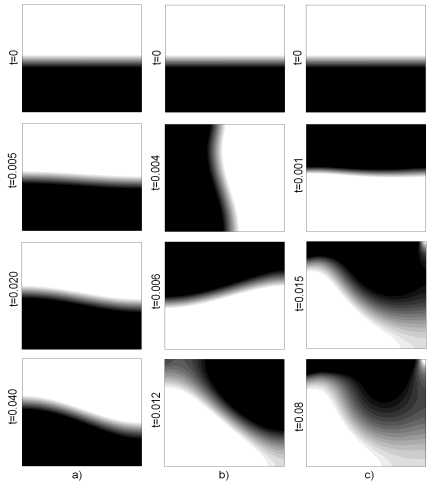

Figure 5: Results of the reaction-convection-diffusion system for a Turing space with a wave number (1,0). The times (dimensionless) are seen in the figure. For a Reynolds number of a) 0.5, b) 5.0 and c) 50.0. The black color indicates high concentration for the variable u, greater than 1.1 (dimensionless). We present only the results of the variable u.

the results only show the level of concentration of u for the reactive system. The variable v has a similar pattern, but with the pattern colors reversed.

3.1 Results for the velocity field in the problem of flow in the cavity

Figure 4 shows the results achieved for the problem of the cavity, which is widely referenced in different papers, such as ([31],[36],[37]). Each row shows the velocity field obtained in the steady state, expressed in each of its components (V_x, V_y), as well as in terms of the resulting, through streamlines. Each row corresponds to the problem solution of the cavity with a non-dimensional velocity in the different upper border: $c = 0.5$, $c = 5.0$ and $c = 50$ (see Figure 4). These values on the boundary are equivalent to a Reynolds number of 0.5, 5.0 and 50.0, respectively. The results show the formation of a vortex in the top center for the two lower velocities, and a vortex in the upper right to the highest speed ($c = 50$). The results of the velocity magnitude in each direction and the resulting pattern agree with the results reported by other authors ([31],[36],[37]). For brevity in the report, Figure 4 do not show the results achieved for the pressure, nor the temporal evolution of the velocity and pressure variables.

These results, and more specifically, the velocity field in the temporal evolution was imposed to the reaction system through the convective term to observe the behavior of Turing patterns to these velocity fields. In the next section we show the results of these numerical tests.

3.2 Results for an initial mode (1,0)

As mentioned above and listed in Table 1, for reaction-diffusion conditions, different values on the coefficients d and γ can generate different Turing patterns, which are identified by their wave number. For example, a Turing pattern with a wave number (1,0) can be obtained from a value $d = 10$ and $\gamma = 29$ (for details see [3]).

Thus, the first case simulated was to evaluate the influence of the advective field derived from the problem of flow in the cavity, in a reaction-diffusion case with $d = 10$ and $\gamma = 29$. The simulation involved from a simple reaction-diffusion problem, allowing its temporary stabilization (this state was taken as $t = 0$), and subsequently adding the advective effects mentioned. Figure 5 show the results of changes in the pattern obtained for the problem described above, using

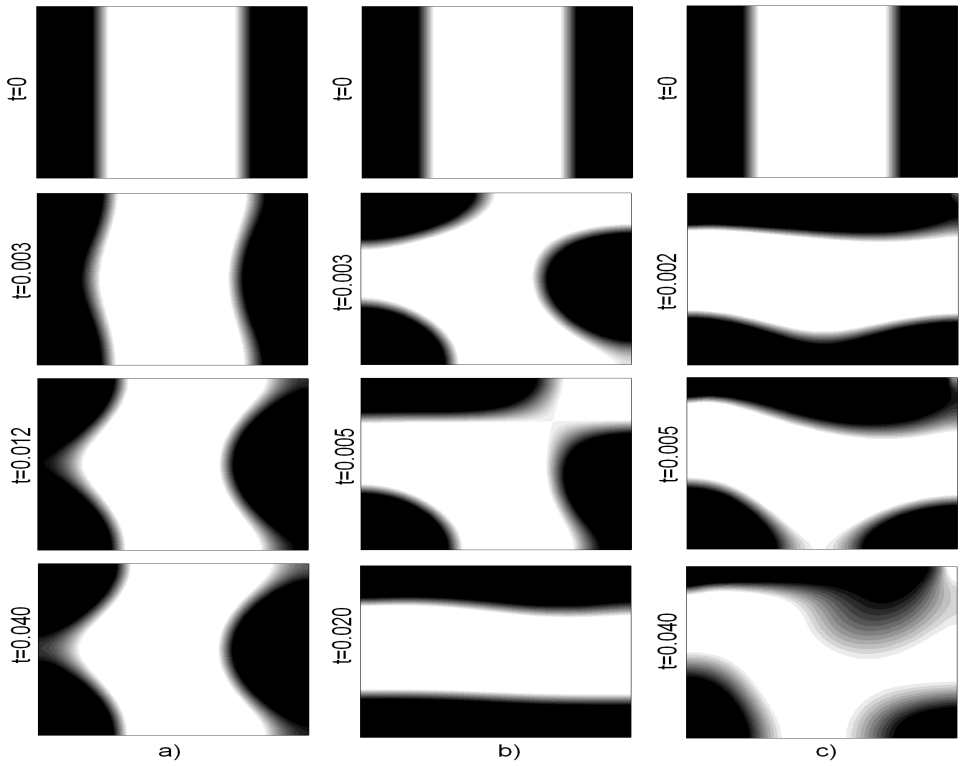

Figure 6: Results of the reaction-convection-diffusion system for a Turing space with a wave number (2,0). The times (dimensionless) are seen in the figure. For a Reynolds number of a) 0.5, b) 5.0 and c) 50.0. The black color indicates high concentration for the variable u. The black color indicates a concentration greater than 1.1 (dimensionless). We present only the results of the variable u.

three velocity fields defined by three different Reynolds numbers: 0.5 (column a) Figure 5), 5.0 (column b) Figure 5) and 50.0 (column c) Figure 5). In the numerical experiment of the column a) in Figure 5 shows the formation of a Turing pattern rotating in the same direction as the velocity field. The new pattern generated is in constant rotation and fails to stabilize at any later time. It should be noted that the density change front moves from being straight to having a curvature as shown in later times.
In Figure 5 b) shows a symmetrical pattern, as in case a), it is in constant rotation in the direction of rotation of the fluid. In Figure 5 c) shows that, at a high velocity, the system reaches a steady state which has a sinusoidal shape after having rotated in the direction of flow. The dimensionless time of stabilization is $t = 0.08$.

3.3 Results for an initial mode (2,0)

Like the previous case, it is taken as the starting point the steady state of the reaction-diffusion problem, imposing then the condition of velocity field. Figure 6 shows the results for the second case of analysis for which we took as parameters $d = 10$ and$\gamma = 114$. In the first row of Figure 6 shows the final state of the reaction-diffusion problem without convection ($t = 0$). Column a) of Figure 6 shows the distortion of the central band of the original pattern. This band is distorted in a semi-arc following the pattern of convective flow, reaching a steady state at t=0.060. Figure 6 b) shows the evolution of a Turing pattern, formed under the effect of a border velocity equal to 5.0. In this test there is a rotation from the original pattern at an angle equal to 90 $^\circ$, along with a small distortion of it. The pattern formed is stable in time and presents a stabilization time t = 0.020. Finally, in column c) in Figure 6, we observed as in case b), a rotation of the original pattern, but with more distortion, which is clearly associated to the advective field. The pattern formed with this velocity is stable temporarily and has a stabilization time t = 0.040.

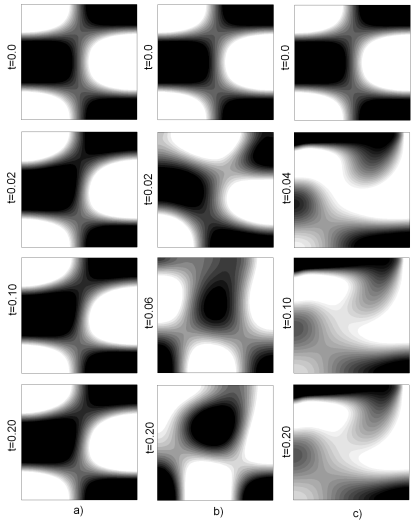

Figure 7: Results of the reaction-convection-diffusion system for a Turing space with a wave number (2,1). The times (dimensionless) are seen in the figure. For a Reynolds number of a) 0.5, b) 5.0 and c) 50.0. The black color indicates high concentration for the variable u. The black color indicates a concentration greater than 1.1 (dimensionless). We present only the results of the variable u.

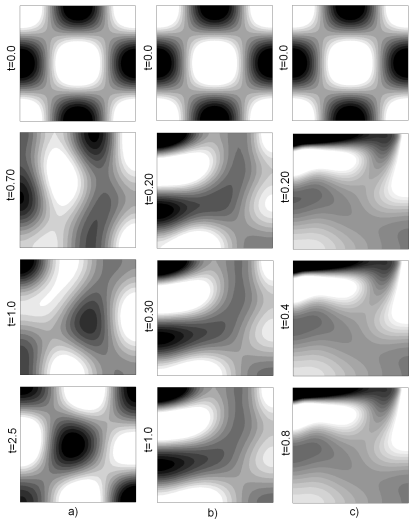

Figure 8: Results of the reaction-convection-diffusion system for a Turing space with a wave number (2,2). The times (dimensionless) are seen in the figure. For a Reynolds number of a) 0.5, b) 5.0 and c) 50.0. The black color indicates high concentration for the variable u. The black color indicates a concentration greater than 1.1 (dimensionless). We present only the results of the variable u.

3.4 Results for an initial mode (2,1)

In this numerical experiment, parameters used correspond to the mode (2,1) in Table 1 and the same three velocity fields used in previous numerical tests. Figure 8 a) shows that the velocity field imposed (Reynolds number equal to 0.5) did not significantly alter the original Turing pattern (formed by the reactive-diffusive effect) only shows a slight distortion, which is stabilized at t = 0.02. Column b) in Figure 8, shows a significant distortion, where the original pattern rotates 90 degrees in direction of the flow. We also observe the formation of a dot whose center coincides with the position of the vortex formed in the fluid (Figure 4 f). The settling time for this case is t=0.020. Column c) in Figure 8 shows that under the effect of a higher advective field (Reynolds number equal to 50.0) the pattern is completely lost, standing two semibandas well established in the top and bottom.

3.5 Results for an initial mode (2,2)

In this numerical test we have established the parameters of reaction and diffusion for a wave number (2,2). Column a) of Figure 9 shows the formation of a Turing pattern under the effect of a low advective field (Reynolds number equal to 0.5), which stabilizes at t=2.5. This new pattern formed consists on the reverse of the original pattern, this is, the areas of high concentration of the original pattern pass, after the application of the convective field, to be areas of low concentration, and viceversa. In column b) and c) in Figure 9 shows a final state that stabilizes at t=1.0 and t=0.8, respectively. We can see that the advective field has totally changed the final pattern in both cases, creating stripes of short length in the upper half of the domain.

3.6 Results for an initial mode (3,3)

Figure 10 shows the results obtained by including advective effect of a Turing pattern mode (3,3). We used three different magnitudes in the velocity field, defined by values in the Reynolds number of 0.50, 5.0 and 50.0, respectively. The patterns obtained for the three cases showed a temporary stabilization at $t = 1.5$, $t = 1.5$ and $t = 0.4$, respectively. In columns a)

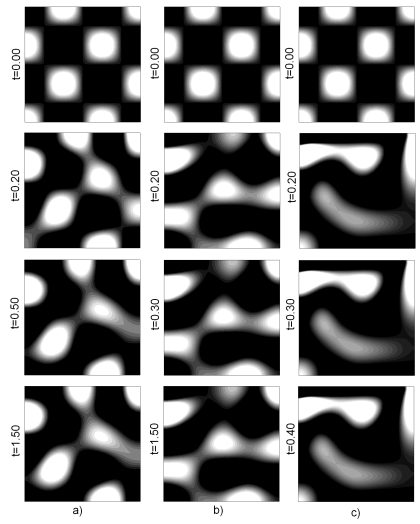

Figure 9: Results of the reaction-convection-diffusion system for a Turing space with a wave number (3,3). The times (dimensionless) are seen in the figure. For a Reynolds number of a) 0.5, b) 5.0 and c) 50.0. The black color indicates high concentration for the variable u. The black color indicates a concentration greater than 1.1 (dimensionless). We present only the results of the variable u.

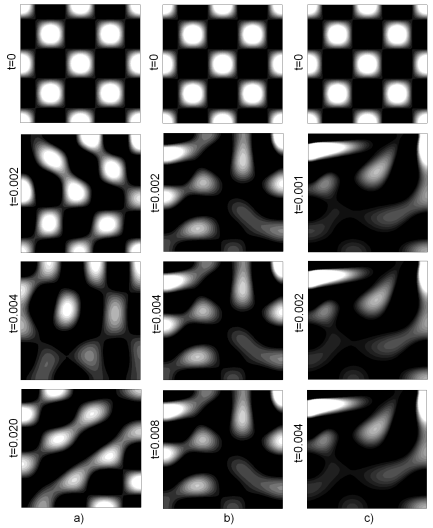

Figure 10: Results of the reaction-convection-diffusion system for a Turing space with a wave number (4,4). The times (dimensionless) are seen in the figure. For a Reynolds number of a) 0.5, b) 5.0 and c) 50.0. The black color indicates high concentration for the variable u. The black color indicates a concentration greater than 1.1 (dimensionless). We present only the results of the variable u.

and b) of Figure 10, there is a loss of the original pattern and the formation of a new pattern characterized by the presence of stripes and spots. For higher values in the advective field, the original pattern is distorted to a greater extent and we observe a pattern formation with two semi-stripes in the domain.

3.7 Results for an initial mode (4,4)

Figure 11 presents the results obtained by introducing the advective field in the reactive-diffusive pattern defined by the parameters $d = 8.6076$ and $\gamma = 909.6600$. For the tests done with three magnitudes of velocity fields (Reynolds number equal to $0.5, 5.0$ and 50.0, respectively) shows that the stationary states are reached at *t=0.020, t=0.008* and $t = 0.004$, respectively. Column a) of Figure 11 shows the formation of oblique stripes, which are the product of the joining spots of the original pattern, also, we note some spots at the bottom, so in general, the pattern is a mixture of spots and stripes. Figure 11 b) shows a pattern of semi-stripes, also generated by the union of the original spots, but exhibiting a distortion generated by the action of the advective field. Finally, in column c) of Figure 11 shows a much more distorted pattern formed by spots and stripes.

3.8 Test of independence of the initial condition

As mentioned, in previous numerical test, the convective term is imposed once the reacrive-diffusive pattern is stabilized, explained by the linear stability theory. In this new test, shown in Figure 12, the parameters are taken for each wave number and the convective term is introduced from random initial conditions and not from the moment of stabilization of the Turing pattern for the reactive-diffusive case. Column a) shows the evolution of the calculated pattern with the same parameters as of the case in Figure 6 c (wave number (1,0)). This numerical test shows no appreciable difference between the now reached steady state and the one exhibited in the case of Figure 6 c. This test of influence of the initial condition is repeated in the trial shown in Figure 12b, calculated with the parameters corresponding to the wave number (4,4). It is found that the steady state achieved, considering as initial condition the steady state of the reactive-diffusive pattern (Figure 11 c), is the same as the initial condition obtained by considering a random distribution of the substance u.

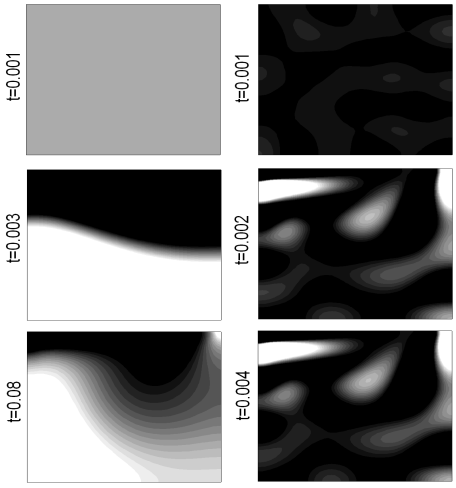

Figure 11: Results of the reaction-convection-diffusion system for a Turing space with wave number (1,0), column a) and (4,4) for column b) In each of these tests the imposed boundary velocity is 5 (dimensionless).

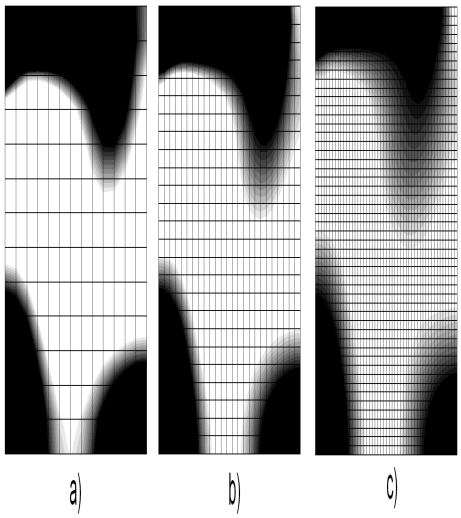

Figure 12: Independence of the mesh a)169 elements, b) 625 elements c) 2500 elements.

3.9 Independence of the mesh

To analyze the influence of the mesh in the shape of the pattern obtained, we computed the problem illustrated in Figure 6 c, with three different meshes: the first with 169 elements, the second with 625 elements and the third with 2500 elements. The results achieved in each mesh are illustrated in Figure 13. As noted in this latter figure, there are no apparent changes in the shape of the pattern, using different mesh sizes. It is to clear out that even with the larger mesh size, we can ensure that the Bubnov-Galerkin formulation implemented allows us to obtain numerically stable solutions.

4 Conclusions

This article has shown several numerical tests for the analysis of Turing pattern formation under the effect of advective field associated with the problem of flow in a cavity ([31],[36],[37]).

The tests done with different parameters of wave number, evidence that the addition of an advective term to the reaction-diffusion equation allows the generation of complex Turing instabilities. In two dimensions, there is the possibility of the emergence of mixed patterns of spots and stripes for strong advective fields. It was found that they may have complex wave pseudo-modes that can change the length and shape of the stripes and spots.

In the case of advective fields of small magnitude, it was noted that the original pattern may in some cases, rotate in the direction of the velocity field, reaching a temporary stabilization or staying in rotation without reaching a steady state (see Figures 5 a and 5 b).

The test done additionally show that the pattern obtained is independent of the initial condition and of the size of the mesh used. In the latter case, it is important to verify that the size of the element used allow us to guarantee a numerically stable solution.

References

[1] D. Garzn. Simulacin de procesos de reaccin-difusin: Aplicacin a la morfognesis del tejido seo. *Universidad de Zaragoza.* 2007.

[2] A. Madzvamuse et al. A moving grid finite element method applied to a model biological pattern generator. *Journal of Computational Physics.* 190(2003): 478–500

[3] A. Madvamuse. A numerical approach to the study of spatial pattern formation. *Oxford University. UK* 2000.
[4] L. Franca and S. Frey. Stabilized finite element methods: II. The incompressible Navier-Stokes equations. *Computer Methods in Applied Mechanics and Engineering.* 99(1992): 209-233.
[5] D. J. Acheson. Elementary Fluid Dynamics, Oxford Applied Mathematics and Computing Science Series. *Oxford University Press.* (1990).
[6] D. White and J. Fluid Mech. The planforms and onset of convection with a temperature dependent viscosity. 191(1988): 247–286.
[7] O. Hirayama and R. Takaki. Thermal convection of a fluid with temperature-dependent viscosity. *Fluid Dynamics Research.* 12(1988)(1): 35-47.
[8] M. Ardes et al. Thermal convection in rotating spherical shells. *Physics of the Earth and Planetary Interiors.* 99(1997): 55-67.
[9] J. Lir and T. Lin. Visualization of roll patterns in Rayleigh–Bénard convection of air in rectangular shallow cavity. *International Journal of Heat and Mass Transfer.* 44(2001): 2889–2902.
[10] Y. Balkarei et al. Regenerative oscillations, spatial-temporal single pulses and static inhomogeneous structures in optically bistable semiconductors. *Opt. Commun.* 66(1988): 161–166.
[11] V. I. Krinsky. Self-organisation: Auto-Waves and structures far from equilibrium. *Ed. Springer.* (1984).
[12] L. Zhang and S. Liu. Stability and pattern formation in a coupled arbitrary order of autocatalysis system. *Applied Mathematical Modelling.* 33(2009): 884–896.
[13] F. Crauste et al. A delay reaction-diffusion model of the dynamics of botulinum in fish. *Mathematical Biosciences*. 216(2008): 17–29.
[14] F. Rossi et al. Dynamics of pattern formation in biomimetic systems. *Journal of Theoretical Biology*. 255(2008): 404–412.
[15] H. Frederik et al. Pigmentation pattern formation in butterflies: experiments and models. 326(2003): 717–727.
[16] F. Yi et al. Bifurcation and spatiotemporal patterns in a homogeneous diffusive predator–prey system. *Journal of Differential Equations.*
[17] M. Baurmanna et ai. Instabilities in spatially extended predator–prey systems: Spatio-temporal patterns in the neighborhood of Turing–Hopf bifurcations. *Journal of Theoretical Biology.* 245(2007): 220–229.
[18] B. Rothschild and J. Ault. Population-dynamic instability as a cause of patch structure. *Ecological Modelling.* 93(1996): 237-239.
[19] T. Nozakura and S. Ikeuchi. Formation of dissipative structures in galaxies. *Astrophys.* 279(1984): 40–52.
[20] A. Madzvamuse. A Numerical Approach to the Study of Spatial Pattern Formation in the Ligaments of Arcoid Bivalves. *Bulletin of Mathematical Biology* 64(2002): 501–530.
[21] J. García-Aznar et al. Computational simulation of fracture healing: Influence of interfragmentary movement on the callus growth. *Journal of Biomechanics.* 40(2007)(7): 1467-1476.
[22] S. Ferreira et al. Reaction-diffusion model for the growth of avascular tumor. *Physical Review.* (2002).
[23] Z. Mei. Numerical Bifurcation Analysis for reaction-diffusion equations. *Springer Verlag. Alemania.* (2000).
[24] Sten Rüdiger et al. Theory of pattern forming systems under traveling-wave forcing. *Physics Reports* 447(2007): 73–111.
[25] F. Sagués et al. Travelling-stripe forcing of Turing patterns. *Physica D: Nonlinear Phenomena.* 199(2004): 235-242.
[26] E. L. Allgower and K. Georg. Numerical path following. *Handbook of Numerical Analysis*. 5(1997): 203-207.
[27] K. J. Painter et al. Stripe formation in juvenile Pomacanthus via chemotactic response to a reaction-diffusion mechanism. *Proceedings of National Academy Sciences USA*. 96(1999): 5549—5554.
[28] K. J. Painter et al. A chemotactic model for the advance and retreat of the primitive streak in avian development. *Bulletin of Mathematical Biology*, 62(2000): 501-525.
[29] A. Madzvamuse. Turing instability conditions for growing domains with divergence free mesh velocity. *Nonlinear Analysis: Theory, Methods & Applications*. 71(2009): 2250-2257.
[30] J. Hoffman. Numerical Methods for Engineers and Scientists. *Mc Graw-Hill. USA.* 1992.
[31] T. Hughes et al. A new finite element formulation for computational and fluid dynamics: V. Circumventing the Babuska-Brezzi condition: a stable Petrov-Galerkin formulation of the Stokes problema accommodating equal-order interpolations. *Computer Methods in Applied Mechanics and Engineering.* 59(1986): 85-99.
[32] T. J. R. Hughes. The Finite Element Method linear Static And Dynamic Finite Element Analysis. Dover. *U.S.A.* (2000).
[33] E. Javierre et al. Numerical modeling of a mechano-chemical theory for wound contraction analysis. *International*

journal of solids and structures. 46(2009): 3597-3606.
[34] O. C. Zienkiewicz and R. L. Taylor. The finite element method. *Butterworth-Heinemann, Oxford*. (2000).
[35] O. Zienkiewicz and R. Taylor. Finite Element Method. *Butterworth-Heinemann College.* 20(2000): 5-150.
[36] T. J. Chung. Computational Fluid Dynamics. *Cambridge University Press.* (2002).
[37] J. Tu and G. H. Yeoh. Computational Fluid Dynamics: A practical Approach. *Ed Butterworth-Heinemann.* (2007).